14th International Symposium on Turbulence and Shear Flow Phenomena (TSFP14)
Heidelberg, Germany, July 28-31, 2026

DATA-DRIVEN CONTROL OF VERY-LARGE-SCALE MOTIONS IN A TURBULENT BOUNDARY LAYER

Mansimran Singh
Department of Mechanical Engineering
University of Alberta
116 St & 85 Ave, Alberta, T6G 2R3, Canada
mansimra@ualberta.ca

Sina Ghaemi
Department of Mechanical Engineering
University of Alberta
116 St & 85 Ave, Alberta, T6G 2R3, Canada
ghaemi@ualberta.ca

ABSTRACT

This study investigates the control of very-large-scale motions (VLSMs) in a turbulent boundary layer (TBL) using active wall deformations as actuation and real-time particle image velocimetry (RT-PIV) as sensing. Two data-driven feedforward control strategies are developed and compared: (i) a joint probability density function (J-PDF) based controller, and (ii) a Wiener filter (WF) based controller. The J-PDF based approach maps upstream velocity fluctuations to wall-normal deformations by minimizing a downstream response metric. A fitted sigmoid function is applied to this J-PDF based mapping to approximate the best response mapping. The WF-based controller is identified from transfer functions linking upstream velocity fluctuations, downstream velocity fluctuations response, and actuation input. Results show that the J-PDF based controller reduces the streamwise turbulence intensity, $\langle u^2\rangle^+$, by approximately 12% within $100 \leq y^+ \leq 150$. The WF-based controller provides slightly stronger overall reduction of streamwise turbulence intensity and achieves a 35% reduction in the VLSM spectral range at $y^+ = 150$ relative to the uncontrolled baseline.

INTRODUCTION

Wall-bounded turbulence remains a central challenge in fluid mechanics due to its direct impact on energy consumption in transportation and industrial systems. Globally, transportation accounts for approximately 30% of all energy consumption worldwide, with a substantial fraction of this energy expended in overcoming viscous and turbulent drag at solid boundaries (International Energy Agency, 2020; Jimenez, 2013). A key challenge and opportunity in turbulent boundary layer (TBL) control is that turbulence hosts a hierarchy of coherent structures spanning a broad range of scales (Kline et al., 1967; Robinson, 1991; Adrian, 2007; Hutchins and Marusic, 2007; Mathis et al., 2009). Active control of turbulence can be designed to exploit the distinct spatial organizations and time scales of specific coherent motions by targeting actuation on these structures rather than attempting to manipulate the full turbulent field.

Since their identification by Kim and Adrian (1999), VLSMs have emerged as promising targets for flow control in high Reynolds number flows because of three key properties. First, they extend over large distances in both the streamwise direction, approximately 10–20δ, and spanwise direction, approximately 0.5δ, where δ is the boundary layer thickness (Adrian, 2007; Hutchins and Marusic, 2007; Dennis and Nickels, 2011). Second, their energy is concentrated at relatively low Strouhal numbers, $0.05 < St < 0.15$, where $St = f\delta/U_\infty$, f is the frequency, and U_∞ is the free-stream velocity (Lee and Sung, 2011). Third, they carry a substantial fraction of the streamwise turbulent kinetic energy and modulate near-wall motions (Mathis et al., 2009). These attributes make VLSMs comparatively accessible targets for real-time sensing and actuation.

While near-wall actuation approaches such as jets (Choi et al., 1994, Abbassi et al., 2017) and spanwise wall motion (Bai et al., 2014) have garnered attention, the present study applies localized wall-normal surface deformation to target VLSM-dominated motions. The appeal of wall-normal deformation is that it injects wall-normal momentum through the wall itself, providing a direct means of interacting with coherent motions without introducing mass flux through the boundary. This distinguishes deformable surface actuation from wall-normal jet forcing, where the introduced mass flux may alter the mean flow or produce undesirable off-wall effects.

Gibeau and Ghaemi (2022, 2023) studied localized wall-deformation using a circular membrane and demonstrated that localized deformations can generate high- and low-speed streamwise velocity fluctuations with streamwise and spanwise scales comparable to VLSMs, without noticeable modification of the mean velocity profile. More recently, Plamondon and Ghaemi (*in preparation*) implemented a simple gain-based feedforward controller using a deformable surface and real-time particle image velocimetry (RT-PIV), reporting reductions in streamwise Reynolds stress in the logarithmic region under opposition control.

Building on the work of Plamondon and Ghaemi (*in preparation*), the present study asks whether data-driven controllers can make more effective use of the same deformable-surface actuator for attenuating VLSM-dominated fluctuations. We use RT-PIV at an upstream location to provide velocity measurements to the controller and construct two feedforward control strategies: a nonlinear best response mapping inferred from a joint-probability-density-function (J-PDF) and a linear Wiener-filter (WF) controller that incorporates a short temporal history of upstream fluctuations to compute the real-time actuation command. In the present work, we focus specifically on these two data-driven controllers because they provide a direct comparison between nonlinear mapping and temporal linear estimation using the same sensing-actuation framework. Controller performance is assessed through changes in the Reynolds stresses of the controlled TBL relative to the uncontrolled baseline.

EXPERIMENTAL METHODOLOGY

Experiments were conducted in a closed-loop wind tunnel with a 6.3:1 contraction feeding a test section of 1.2 m × 2.4 m cross section. A TBL developed along the smooth bottom wall

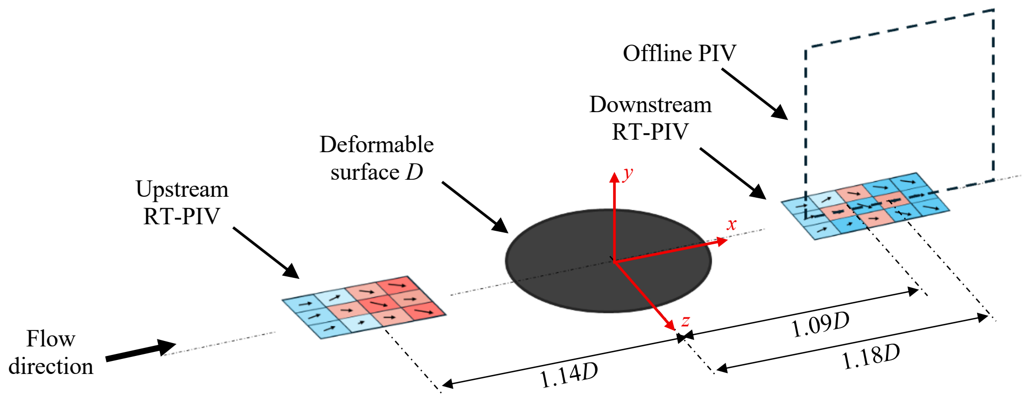

Figure 1: Schematic of the experimental arrangement, showing the active deformable surface and PIV fields of view. Offline-PIV is acquired in the *x*-*y* plane; upstream and downstream RT-PIV planes are acquired in the *x*-*z* frame.

at a freestream velocity of U_∞ = 12.1 ms^{-1}, corresponding to a friction Reynolds number, $Re_\tau \approx 2600$. The active surface was mounted flush with the floor and located 7.6 m downstream of a boundary-layer tripping device to ensure adequate streamwise development. A Cartesian coordinate system (x, y, z) is defined with its origin at the centre of the undeformed active surface, where x, y, and z denote the streamwise, wall-normal, and spanwise directions, respectively, as shown in Figure 1.

Actuator

The active surface is identical to that used by Plamondon and Ghaemi (*in preparation*), schematically shown in Figure 2. Wall-normal deformation was produced using a high-excursion voice coil actuator (VCA) mounted beneath a thin circular silicone membrane installed flush to the wind-tunnel floor. The free to deform membrane diameter was D = 100 mm, approximately equal to the local boundary layer thickness, δ = 98.7 mm. The actuator drove the membrane through a rigid shaft connected to a load-distribution disk of diameter $d = 0.5D$ which spread the imposed displacement and smoothed the transition between the deformed membrane and the surrounding undeformed wall. The actuator produced wall-normal displacements up to ± 0.07δ, where h = 0 corresponds to the membrane being flush with the wall.

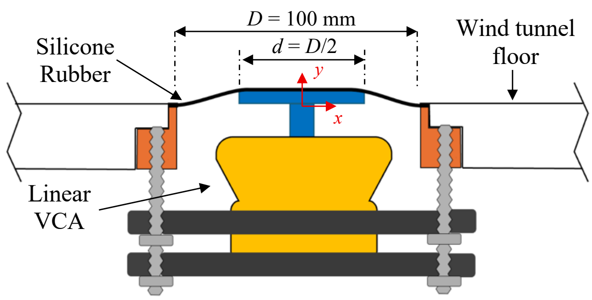

Figure 2: Cross-sectional schematic of the active surface mounted flush with the wind-tunnel floor producing upward wall-normal displacement $h(t)$ relative to undeformed wall (h > 0).

Offline - PIV

Planar PIV measurements in the *x*-*y* plane were carried out along the actuator centreline (z = 0) at x = 1.18D (Figure 1). These measurements are referred to as offline – PIV to distinguish them from the RT-PIV system used for control. Offline PIV was acquired at a sampling frequency of 7.5 Hz with a field of view of approximately 26 mm × 54 mm. A dual cavity Nd: YAG laser was used with an interframe time of Δt = 65 µs, corresponding to a maximum pixel displacement of approximately 14 pixels. Velocity vectors were computed in DaVis 8.4 (LaVision GmbH) using a multi-pass cross-correlation procedure, with a final 32 × 32 Gaussian-weighted interrogation window (IW) and 75% overlap, giving a vector spacing of 0.37 mm vector^{-1}, or equivalently 9.8δ_v vector^{-1}, where δ_v is the viscous length scale.

Real time – PIV

RT-PIV measurements were acquired in two streamwise-spanwise (x-z) planes centred at the actuator centreline (z = 0) and fixed at y^+ = 150, corresponding to $y \approx 5.5$ mm. The upstream plane is centred at x = -1.14D and spans 0.11D × 0.09D in x and z, respectively. The upstream plane provided the feedforward sensing input to the controller. The downstream plane was centred at x = 1.09D and spans 0.14D × 0.09D in x and z, respectively. The downstream plane was used for controller development and response quantification. Although both planes were acquired synchronously, only the upstream plane was processed on the real-time control path because all controllers considered here were strictly feedforward.

Image acquisition. Image acquisition was performed using two high-speed cameras (Basler ace 2), with one camera dedicated to each plane. Image pairs were acquired at f_s = 400 Hz with an inter-pulse separation of Δt = 70 µs. Real-time velocity fields in the upstream plane were computed using a single-pass cross-correlation with 64 × 64 -pixel interrogation windows and no overlap. Prior to each real-time experiment, 24,000 upstream image-pairs were collected to compute the mean velocity field, $\bar{U}_u$ (x, z). During real-time operation, the instantaneous upstream velocity field, U_u (x, z, t) was converted to a fluctuation field, u_u (x, z, t) = U_u (x, z, t) - $\bar{U}_u$ (x, z). The upstream fluctuation field was spatially averaged over the RT-PIV vector grid.

Timing and latency. The real-time control system synchronized image acquisition, PIV processing, and actuation output. The two RT-PIV cameras were triggered at 800 Hz to produce double-frame image pairs. The images were illuminated using a dual-cavity laser that generated pulses separated by 70 μs. The total control path latency τ_L was decomposed as $\tau_L = \tau_{acq} + \tau_{proc} + \tau_{filter} + \tau_{out}$, where τ_{acq} is the image acquisition and transfer time, τ_{proc} is the RT-PIV processing time, τ_{filter} is the temporal filter group delay, and τ_{out} includes DAC update and actuator electromechanical response. Image transfer over USB 3.0 required approximately 2.8 ms, while GPU-accelerated PIV processing required approximately 1 ms per upstream image pair. The actuator delay was approximately 5.2 ms, including the DAC update and electromechanical delay. The resulting latency was approximately 9 ms. The VLSM advection time was estimated using $U_C \approx \bar{U}_u$ ($y^+ = 150$), consistent with previous observations that the convection velocity of outer-layer turbulent structures is well approximated by the local mean velocity (Lee and Sung, 2011). The present $y^+ = 150$ location gives $U_C \approx 0.74 U_\infty$, yielding an advection time from the upstream sensing plane to the actuator of approximately 12.7 ms. A 3rd order temporal causal FIR filter was applied, which added an extra 3.75 ms of delay to the control path latency, equating τ_L to the advection delay.

Asynchronous data collection

For controller development, baseline unforced and randomly forced datasets were collected. The baseline dataset was acquired with no actuation and consisted of 5.04×10^5 vector fields per RT-PIV plane at $f_s = 400$ Hz. The randomly forced dataset was acquired by driving the actuator independently of the upstream flow using band-limited random signals. For each run, a white-noise sequence was generated, transformed to the frequency domain, truncated to retain components within a prescribed frequency band, and inverse-transformed to obtain a real-valued actuator command. The forcing band was varied across runs within $0.1 \leq f \leq 50$ Hz, and the peak-to-peak displacement amplitude was randomized between 2 mm and 14 mm. The dataset included synchronized upstream RT-PIV, downstream RT-PIV, and actuator-command measurements, yielding approximately 1.2×10^6 temporal instances. The downstream fields from the asynchronous dataset were processed offline using a final 32 × 32-pixel IW with 75% overlap.

CONTROLLERS

The controllers implemented in this study share the same sensing and actuation architecture and differ only in the mapping from upstream velocity fluctuation to wall-normal deformation. Each controller generates a deformation command $h(t)$ within the actuator limits $|h| \leq 0.07\delta$. The two controllers considered here are: (i) a nonlinear J-PDF based best-response controller, and (ii) a linear Wiener-filter-based feedforward controller.

J-PDF-based best-response controller

For the J-PDF based controller, the upstream RT-PIV field $u_u(x, z, t)$ was spatially averaged and temporally filtered to $\langle u_u \rangle_{xz',filt}(t)$. Since the actuator response lags the upstream measurement by the measured control-path latency, the deformation paired with an upstream state at time t is taken as $h(t + \tau_L)$. The downstream response is evaluated at a delay $\tau_{ud} = 25$ ms, corresponding to the advection time between the upstream and downstream RT-PIV planes. The downstream response metric is $\langle u_d^2 \rangle_{xz}/u_\tau^2$, where $\langle \cdot \rangle_{xz}$ denotes spatial average over the downstream measurement window. The randomly sampled dataset therefore provides grouping of the form $(\langle u_u \rangle_{xz',filt}(t), h(t + \tau_L), \langle u_d^2 \rangle_{xz}/u_\tau^2 (t + \tau_{ud}))$. These samples are used to construct a bin-averaged downstream response map over upstream state and actuation. The range of $\langle u_u \rangle_{xz',filt}(t)$ is divided into 31 overlapping bins spanning [-1.5, 1.5] m s^{-1}, while the range of h was partitioned into 31 overlapping bins spanning [-7, 7] mm. For each bin pair (B_i, C_j), the mean downstream response is computed from all samples falling within that pair.

The best response deformation for each upstream bin is then selected as the actuation value that minimizes the bin averaged downstream response. This produces a discrete set of optimal deformation values, represented by the red line in Figure 3, which are fitted by using a bounded sigmoid function,

$$h = h_{min} + \frac{h_{max} - h_{min}}{1 + \exp\left[-a\left(\langle u_u \rangle_{xz',filt} - s_0\right)\right]}, \quad (1)$$

and represented with the black fitted line in Figure 3. Here h_{min} and h_{max} are the lower and upper saturation levels, a controls the transition steepness, and s_0 is the upstream value at the inflection point. For the present dataset, the fitted parameters are $h_{min} = -4.3$ mm, $h_{max} = 5.6$ mm, $a = 2.7$, and $s_0 = 0.46$ m s^{-1}. The colour field of Figure 3 represents the expected value of $\langle u_d^2 \rangle_{xz}/u_\tau^2$ associated with applying h for a given $\langle u_u \rangle_{xz',filt}$.

Two features of Figure 3 stand out. First, the best-response map shows a clear low $\langle u_d^2 \rangle_{xz}/u_\tau^2$ valley in the $(\langle u_u \rangle_{xz',filt}, h)$ plane. Negative upstream fluctuations favour negative wall-normal displacement, while positive upstream fluctuations favour positive displacement. This indicates that the best-response map follows a u-opposition sign logic, but not a simple symmetric proportional gain relationship. Second, the mapping is nonlinear and saturates toward bounded plateaus as $|\langle u_u \rangle_{x'z,filt}|$ increases. Beyond moderate deformation amplitudes, further increases in $|h|$ do not appear to provide additional reductions in $\langle u_d^2 \rangle$ and may instead introduce penalties, as indicated by the higher response toward the top-right and bottom-left corners of the map. This is consistent with findings of Plamondon and Ghaemi (*in preparation*), who found that increasing actuation strength beyond moderate levels did not produce favourable reductions in the downstream response.

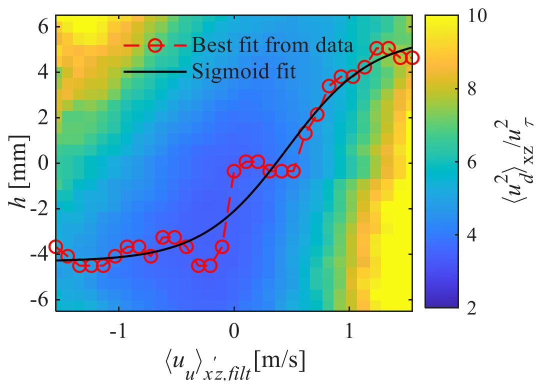

Figure 3: Bin-averaged downstream response computed as the mean value of $\langle u_d^2 \rangle_{xz}/u_\tau^2$ over all samples falling within each bin B_i and actuation bin C_j. Red circles denote the minimum response actuation selected for each upstream bin, and the black curve shows the fitted sigmoid control law.

Wiener filter-based controller

The WF-based controller uses a linear input-output framework to predict and attenuate downstream large-scale streamwise fluctuations (Rathnasingham and Breuer, 1997, 2003; Dacome et al., 2024). The approach assumes that over the short advection interval between the upstream sensing plane, actuator, and downstream evaluation plane, the large-scale component of the flow can be approximated using linear transfer functions. This provides a feedforward control law that incorporates a short temporal history of upstream measurements.

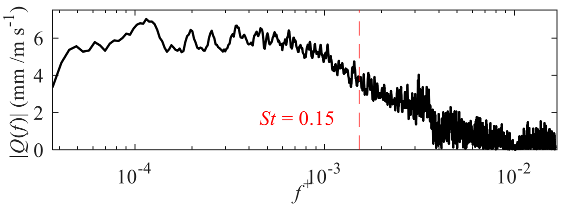

Figure 4: Construction of the Wiener feedforward kernel showing magnitude of $\hat{Q}(f)$. The vertical dashed line marks St = 0.15.

For this controller, the upstream and downstream RT-PIV fields are spatially averaged to obtain $\langle u_u \rangle_{xz}(t)$ and $\langle u_d \rangle_{xz}(t)$. No temporal low-pass FIR filter is applied before identification, since the relevant temporal weighting is captured by the identified kernels. First, the baseline relationship between upstream and downstream fluctuations is estimated from the unforced dataset. In the absence of actuation, the downstream signal is modelled as $\langle u_d \rangle_{xz}(t) \approx Z(t) * \langle u_u \rangle_{xz}(t)$, where $Z(t)$ is a linear transfer function and * denotes convolution. In the frequency domain, the corresponding Wiener estimate is

$$\hat{Z}(f) = S_{\langle u_u \rangle_{xz} \langle u_d \rangle_{xz}}(f) / S_{\langle u_u \rangle_{xz} \langle u_u \rangle_{xz}}(f), \quad (2)$$

where $S_{\langle u_u \rangle_{xz} \langle u_d \rangle_{xz}}$ is the cross-power spectral density (CPSD) between $\langle u_u \rangle_{xz}$ and $\langle u_d \rangle_{xz}$, and $S_{\langle u_u \rangle_{xz} \langle u_u \rangle_{xz}}$ is the auto-power spectral density (PSD) of $\langle u_u \rangle_{xz}$. The $\langle u_d \rangle_{xz}(t)$ is then modelled as superposition of natural convection of upstream flow and actuator induced contribution,

$$\langle u_d \rangle_{xz}(t) = Z(t) * \langle u_u \rangle_{xz}(t) + H(t) * h(t), \quad (3)$$

where $H(t)$ is the actuation deformation to downstream flow transfer function. The actuator-induced component is isolated using the residual $\varepsilon_d(t) \approx \langle u_d \rangle_{xz}(t) - Z(t) * \langle u_u \rangle_{xz}$, so that $\varepsilon_d(t) \approx H(t) * h(t)$. The transfer function $\hat{H}(f)$ is then estimated from the randomly forced dataset using,

$$\hat{H}(f) = S_{\epsilon_d h}(f) / S_{hh}(f). \quad (4)$$

The feedforward objective of this controller is to choose $h(t)$ such that the actuator induced response cancels the downstream fluctuation predicted from the upstream measurement. This gives $- Z(t) * \langle u_u \rangle_{xz}(t) \approx H(t) * h(t)$. The frequency domain controller is therefore obtained using the inverse,

$$\hat{Q}(f) = -\hat{Z}(f) / \hat{H}(f)\,. \quad (5)$$

The real-time actuation command is then computed from the time-domain FIR kernel $q[n]$,

$$h[t] = \sum_{n=0}^{L-1} q[n] \langle u_u \rangle_{xz}[t-n]. \quad (6)$$

The magnitude of $|\hat{Q}(f)|$ is largest at low frequencies and becomes increasingly irregular at higher frequencies. To avoid implementing this high-frequency irregularity, the controller was converted to a time-domain FIR kernel and truncated to the first 113 coefficients, corresponding to 95% of the cumulative coefficient energy.

RESULTS

The controller performance is first evaluated using the downstream Reynolds-stress profiles shown in figure 5, followed by the spectral responses in figures 6 and 7. This allows the wall-normal distribution of stress changes to be interpreted alongside the frequency range over which each controller acts.

Figure 5 compares the downstream Reynolds stress profiles for the uncontrolled baseline, the J-PDF based controller, and the WF-based controller. The upper panel (a) shows the viscous-scaled Reynolds stresses, while the lower panels, (b – d) show the corresponding fractional changes relative to the baseline for $\langle u^2 \rangle^+$, $\langle v^2 \rangle^+$, and $\langle uv \rangle^+$. The reduction in $\langle u^2 \rangle^+$ is evident for both controllers in Figure 5(b). The J-PDF based controller produces a peak reduction of approximately 13% near $y^+ \approx 130$, with an integrated reduction of approximately 9% over $20 \le y^+ \le 260$. The WF-based controller provides a slightly stronger attenuation, with $\langle u^2 \rangle^+$ reduced by approximately 10.0% over $20 \le y^+ \le 260$.

The change in the other Reynolds-stress components shows a clearer distinction between the two controllers. As shown in Figure 5(c), both controllers increase $\langle v^2 \rangle^+$ in the lower logarithmic region, but the increase is larger for the WF controller. Over $20 \le y^+ \le 260$, the J-PDF controller produces an integrated increase of approximately 6.0%, whereas the WF controller increases $\langle v^2 \rangle^+$ by approximately 9.7%. A similar trend is observed for $\langle uv \rangle^+$ in Figure 5(d). The J-PDF controller leaves $\langle uv \rangle^+$ nearly unchanged over $20 \le y^+ \le 260$, while the WF controller introduces a modest increase of approximately 3.8%. These stress increases decay further from the wall, indicating that the main penalty remains localized to the lower logarithmic region.

Figure 6 and

Figure **7** provide spectral context for the observed Reynolds-stress changes at $y^+ = 150$. Figure 6(a) shows the pre-multiplied streamwise and spanwise spectra for the baseline and J-PDF controlled cases. The J-PDF controller reduces the streamwise spectral energy primarily at low frequencies, below the $St = 0.15$ marker. Figure 6(b) shows the relative percentage difference in the premultiplied spectra between controlled case (i.e. $\phi_{uu,cont}$), and the uncontrolled (i.e. $\phi_{uu,base}$), following

$$\Delta\phi(\%) = \frac{\phi_{uu,cont} - \phi_{uu,base}}{\phi_{uu,base}} \times 100\% \quad (7)$$

The streamwise spectral reduction in the low-frequency range is approximately 27%. This is coincident with the VLSM range. Here, the relative difference in spectral energy in relation to the baseline at that frequency shows a consistent drop in streamwise Reynolds stress. This confirms that the deformable actuator, and specifically J-PDF controller mainly attenuate the intended large-scale contribution, while adding negligible collateral high frequency energy to the flow.

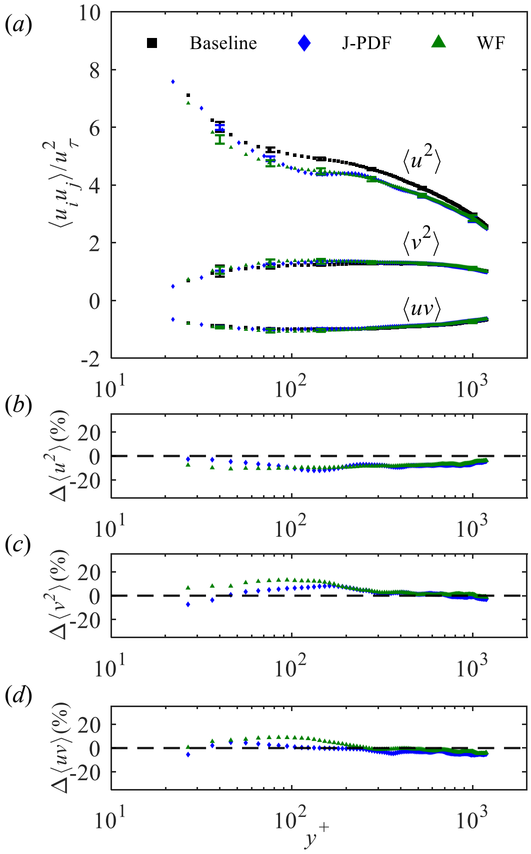

Figure 5. Reynolds-stress response for the uncontrolled baseline (black), J-PDF based controller (blue), and WF-based controller (green). (*a*) Viscous-scaled Reynolds stress profiles, including $\langle u^2\rangle^+$, $\langle v^2\rangle^+$, and $\langle uv\rangle^+$. Error-bars indicate the range over three repeated runs under identical conditions. (*b* - *d*) Fractional changes relative to the uncontrolled baseline for $\langle u^2\rangle^+$, $\langle v^2\rangle^+$, and $\langle uv\rangle^+$, respectively.

The spanwise spectral response, $f\phi_{ww}/u_\tau^2$ of baseline and J-PDF controller in Figure 6(*b*) remains close over the frequency range, with only modest increases across the frequency spectrum. Overall, the $\Delta\phi_{ww}$(%) increase in the controlled case averages to 5% over the frequency range at $y^+ = 150$.

Figure 7 shows the corresponding spectral response for the WF-based controller. Similar to the J-PDF case, the WF controller reduces streamwise energy primarily below the St = 0.15 marker. However, the low-frequency reduction is slightly larger, at approximately 35% for the low-frequency range. At higher frequencies, the WF controller also results in slightly higher streamwise spectral energy content than the J-PDF controller. The spanwise spectrum in

Figure **7**(*b*) shows a modest increase under WF control, with $\Delta\phi_{ww}$ (%) increasing by approximately 9% over the measured frequency range. Together with $\langle v^2\rangle^+$ and $\langle uv\rangle^+$ increases in Figure 5, this indicates that the stronger streamwise attenuation from the WF controller is accompanied by somewhat larger secondary effects than those observed for the J-PDF controller.

Overall, Figure 5, Figure **6**, and

Figure **7** show that both data-driven feedforward controllers successfully attenuate VLSM-scale streamwise energy using localized wall-normal deformation. The J-PDF controller provides a nonlinear memoryless mapping that reduces $\langle u^2\rangle^+$ while limiting changes in $\langle v^2\rangle^+$, $\langle uv\rangle^+$, and ϕ_{ww}. The WF controller, by incorporating temporal history of the upstream signal, produces the strongest streamwise attenuation and the largest low-frequency spectral reduction, but with slightly larger increases in the secondary stress components. This suggests a trade-off between attenuation strength and component selectivity.

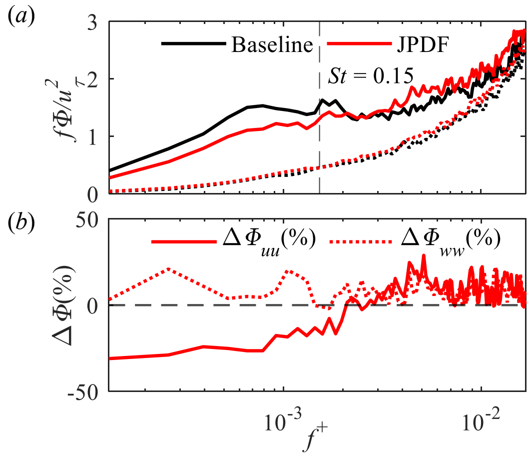

Figure 6. Spectral response of the J-PDF based controller at y^+ = 150. (*a*) Pre-multiplied streamwise and spanwise spectra for the uncontrolled baseline and J-PDF controlled case. Solid lines show $f\phi_{uu}/u_\tau^2$, and dotted lines show $f\phi_{ww}/u_\tau^2$. The vertical dashed line marks St = 0.15, taken as the upper limit of the VLSM dominated frequency range. (*b*) Percentage difference in premultiplied spectra between the J-PDF controlled and uncontrolled baseline cases.

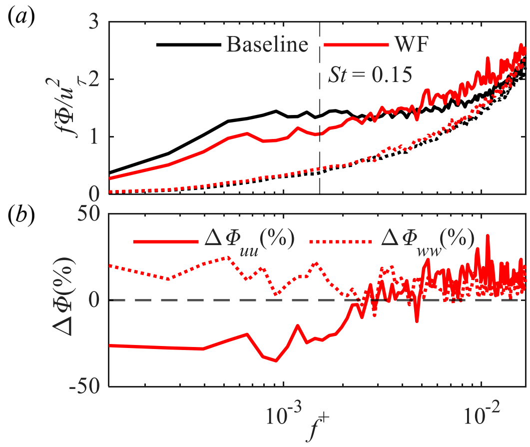

Figure 7. Spectral response of the WF-based controller at y^+ = 150. (*a*) Pre-multiplied streamwise and spanwise spectra for the uncontrolled baseline and WF controlled case. Solid lines show $f\phi_{uu}/u_\tau^2$, and dotted lines show $f\phi_{ww}/u_\tau^2$. The vertical dashed line marks St = 0.15, taken as the upper limit of the VLSM dominated frequency range. (*b*) Percentage difference in premultiplied spectra between the WF-controlled and uncontrolled baseline cases.

CONCLUSION

This study experimentally evaluated feedforward control of VLSM-dominated motions in a TBL using localized wall-normal surface deformations. Experiments were performed at $Re_\tau \approx 2600$ using upstream RT-PIV sensing at $y^+ = 150$, a circular deformable surface with diameter $D \approx \delta$, and downstream response measurements from both offline PIV and RT-PIV. Two data-driven control strategies were implemented and compared: a nonlinear J-PDF-based best-response controller and a Wiener-filter-based feedforward controller incorporating temporal history of the upstream signal.

Both controllers reduced the downstream streamwise Reynolds stress relative to the uncontrolled baseline. The J-PDF based controller produced a peak reduction of approximately 13% in $\langle u^2 \rangle^+$ near $y^+ = 130$, with an integrated reduction of 9.0% over $20 \leq y^+ \leq 260$. Spectral analysis showed that the J-PDF controller primarily reduced low-frequency streamwise energy associated with the targeted VLSM range, with a reduction of approximately 27% below the St = 0.15 marker. The WF controller produced slightly stronger streamwise attenuation. The reduction in $\langle u^2 \rangle^+$ remained approximately 12% over $20 \leq y^+ \leq 260$. The corresponding low-frequency spectral reduction was approximately 35%.

Taken together, these results demonstrate the value of both nonlinear and history aware feedforward control for attenuating VLSM dominated motions. The J-PDF based controller provides a bounded nonlinear mapping that departs from a symmetric proportional-gain law, allowing the deformation amplitude to saturate once further actuation no longer produces additional benefit. The WF-based controller uses temporal history in the upstream signal to shape the actuation command toward the large-scale, lower-frequency motions targeted in this study. These findings suggest that future controllers may benefit from combining both features: nonlinear response shaping and causal use of upstream history. Future work should therefore examine nonlinear history-aware control strategies to determine the achievable limits of VLSM attenuation using localized wall-normal deformable surface actuation.

REFERENCES

International Energy Agency, 2020, *World Energy Outlook 2020*, IEA, Paris.

Jiménez, J., 2013, "Near-wall turbulence," *Physics of Fluids*, Vol. 25, p. 101302.

Kline S. J., Reynolds W. C., Schraub F. A., Runstadler P.W., 1967, "The structure of turbulent boundary layers". *Journal of Fluid Mechanics*, Vol. 30, pp. 741-773.

Robinson S.K., 1991, "Coherent Motions in the Turbulent Boundary Layer". *Annual Review of Fluid Mechanics*, Vol. 23, pp. 601-639.

Adrian R.J., 2007, "Hairpin vortex organization in wall turbulence". *Physics of Fluids*, Vol. 19, pp. 041301.

Hutchins N., Marusic I., 2007, "Evidence of very long meandering features in the logarithmic region of turbulent boundary layers". *Journal of Fluid Mechanics*, Vol. 579, pp. 1-28.

Mathis R., Hutchins N., Marusic I., 2009, "Large-scale amplitude modulation of the small-scale structures in turbulent boundary layers". *Journal of Fluid Mechanics*, Vol. 628, pp. 311-337.

Kim K. C., Adrian R.J., 1999, "Very large-scale motion in the outer layer". *Physics of Fluids*, Vol. 11, pp. 417-422.

Dennis D. J. C., Nickels T.B., 2011, "Experimental measurement of large-scale three-dimensional structures in a turbulent boundary layer. Part 2. Long structures". *Journal of Fluid Mechanics*, Vol. 673, pp. 218-244.

Lee J. H., Sung H. J., 2011, "Very-large-scale motions in a turbulent boundary layer". *Journal of Fluid Mechanics*, Vol. 80, pp. 80-120.

Choi H., Moin P., Kim J., 1994, "Active turbulence control for drag reduction in wall-bounded flows". *Journal of Fluid Mechanics*, Vol. 262, pp. 75-110.

Abbassi M.R., Baars W.J., Hutchins N., Marusic I., 2017, "Skin-friction drag reduction in a high-Reynolds-number turbulent boundary layer via real-time control of large-scale structures". *International Journal of Heat and Fluid Flow*, Vol. 67, pp. 30-41.

Bai H. L., Zhou Y., Zhang W. G., S. J. Xu, Y. Wang, Antonia R. A., 2014, "Active control of a turbulent boundary layer based on local surface perturbations". *Journal of Fluid Mechanics*, Vol. 750, pp. 316-354.

Gibeau B., Ghaemi S., 2022, "Laminar boundary layer forcing with active surface deformations". *Physics Review Fluids*, Vol. 7, pp. 114101.

Gibeau B., Ghaemi S., 2023, "Manipulation of a turbulent boundary layer using active surface deformations". *Journal of Fluid Mechanics*, Vol. 966, pp. A6.

Plamondon C., Ghaemi S., "Feedforward control of very-large-scale motions using wall deformations and real-time image velocimetry. *In preparation.*

Rathnasingham R., Breuer K. S., 1997, "System identification and control of a turbulent boundary layer". *Physics of Fluids*, Vol. 9, pp. 1867-1869.

Rathnasingham R., Breuer K. S., 2003, "Active control of turbulent boundary layers". *Journal of Fluid Mechanics*, Vol. 495, pp. 209-233.

Dacome G., Mörsch R., Kotsonis M., Baars W. J., 2024, "Opposition flow control for reducing skin-friction drag of a turbulent boundary layer". *Physics Review Fluids*, Vol. 9.